



# Induced nanoparticle aggregation for short nucleic acid quantification by depletion isotachophoresis



Steven Marczak, Satyajyoti Senapati, Zdenek Slouka<sup>1</sup>, Hsueh-Chia Chang\*

Department of Chemical and Biomolecular Engineering, University of Notre Dame, 182 Fitzpatrick Hall, Notre Dame Avenue, Notre Dame, IN, 46556 United States

## ARTICLE INFO

### Article history:

Received 10 March 2016

Received in revised form

31 May 2016

Accepted 26 July 2016

Available online 27 July 2016

### Keywords:

Ion-selective membrane

Isotachophoresis

Nanoparticle aggregation

Nucleic acid

## ABSTRACT

A rapid (<20 min) gel-membrane biochip platform for the detection and quantification of short nucleic acids is presented based on a sandwich assay with probe-functionalized gold nanoparticles and their separation into concentrated bands by depletion-generated gel isotachophoresis. The platform sequentially exploits the enrichment and depletion phenomena of an ion-selective cation-exchange membrane created under an applied electric field. Enrichment is used to concentrate the nanoparticles and targets at a localized position at the gel-membrane interface for rapid hybridization. The depletion generates an isotachophoretic zone without the need for different conductivity buffers, and is used to separate linked nanoparticles from isolated ones in the gel medium and then by field-enhanced aggregation of only the linked particles at the depletion front. The selective field-induced aggregation of the linked nanoparticles during the subsequent depletion step produces two lateral-flow like bands within 1 cm for easy visualization and quantification as the aggregates have negligible electrophoretic mobility in the gel and the isolated nanoparticles are isotachophoretically packed against the migrating depletion front. The detection limit for 69-base single-stranded DNA targets is 10 pM (about 10 million copies for our sample volume) with high selectivity against nontargets and a three decade linear range for quantification. The selectivity and signal intensity are maintained in heterogeneous mixtures where the nontargets outnumber the targets 10,000 to 1. The selective field-induced aggregation of DNA-linked nanoparticles at the ion depletion front is attributed to their trailing position at the isotachophoretic front with a large field gradient.

© 2016 Elsevier B.V. All rights reserved.

## 1. Introduction

Recently, genomic diagnosis and prognosis liquid biopsies involving detection of fragmented circulating tumor DNA (ctDNA) and messenger RNA (mRNA) as well as quantification of microRNA (miRNA) expression levels have been proposed for numerous diseases, disorders, and cancers (Calin and Croce, 2006; Lujambio and Lowe, 2012; Vogelstein et al., 2013). These are short nucleic acids with the shortest being single-stranded miRNA which are typically 19–26 nucleotides in length. Current genomic biopsy detection and quantification techniques are microarray and PCR based. Other than sample cost and reliance on lab-bound

equipment and trained personnel, both techniques suffer from long assay times due to diffusion to the surface bound probes for the microarrays and extensive pretreatment to eliminate inhibitors in PCR. Thus, there has been a continuous search for new, simple, rapid quantification methods for low-resource settings that do not require extensive pretreatment (Slouka et al., 2014). More importantly, variations in amplification efficiency and non-target interference significantly compromise the quantification accuracy of PCR and microarray techniques, respectively. A highly selective PCR-free technique, similar to the lateral flow immunoassay but with quantification capability, would be the ideal platform.

Plasmonic nanoparticles, first reported for use as selective DNA sensors by Elghanian et al. (1997), are an essential feature in most lateral flow devices which traditionally detect proteins (Parolo et al., 2013; Fang et al., 2011; Hampl et al., 2001) but increasingly focus on nucleic acids (Mao et al., 2009; He et al., 2011; Chua et al., 2011; Rohrman et al., 2012; Gao et al., 2014; Hou et al., 2012; Hu et al., 2013). Their attractiveness lies in their simplicity, yet their

\* Corresponding author.

E-mail addresses: [smarczak@nd.edu](mailto:smarczak@nd.edu) (S. Marczak), [satyajyoti.senapati.1@nd.edu](mailto:satyajyoti.senapati.1@nd.edu) (S. Senapati), [sloukaz@vscht.cz](mailto:sloukaz@vscht.cz) (Z. Slouka), [hchang@nd.edu](mailto:hchang@nd.edu) (H.-C. Chang).

<sup>1</sup> Present Address: Department of Chemical Engineering, University of Chemistry and Technology, Technická 3, Prague 6 16628, Czech Republic.

primary drawbacks include low sensitivities and poor limits of detection. Several strategies attempting to overcome these limitations are use of upconverting nanoparticles (Hampl et al., 2001; Corstjens et al., 2003), amplification by enzymatic reaction (Parolo et al., 2013), or isotachophoretic concentration (Moghadam et al., 2015). However, because the immobilized probes are often insufficiently selective (de Avila et al., 2013) and the isolation of targets based on mobility differences is inadequate, lateral flow assays, which tend to be only semi quantitative, are nearly always limited to detection of a single target at high concentration and lack mechanisms to improve specificity such as shear by hydrodynamic flow or by electric fields.

In contrast, gel electrophoresis is a very common procedure for separating and detecting multiple analytes and is routinely used in the lab to identify PCR products (Traver et al., 2014) and other nucleic acid samples quantitatively through Northern blotting. Gel separations of probe-functionalized nanoparticles, though, have been confined mostly to slab gel electrophoresis wherein various groups purified polydisperse nanoparticle mixtures based on their characteristic size, shape, charge, and functional molecules (Xu et al., 2007; Hanauer et al., 2007; Wu et al., 2013; Hlavacek et al., 2014; Kim et al., 2013). Capillary electrophoresis was also used for separating nanoparticles (Liu and Wei, 2004; Liu et al., 2005; Liu, 2009) but for purposes of characterization rather than detection. Notably lacking from previous research are techniques which take advantage of nanoparticles' size and shape properties to separate and detect small molecules with similar sizes such as short DNAs and RNAs. Although gel electrophoresis lacks the capacity to separate different sequences with identical numbers of base pairs, these sequences can be separated based on the physical and chemical properties of the nanoparticles themselves. In principle, isotachophoresis with two electrolytes of different ionic strength can also achieve nanoparticle concentration and isolation in a gel medium or in a capillary, and there are a few groups who worked on such applications (Pyell et al., 2009; Hlavacek and Skladal, 2012; Praus et al., 2015) but without realizing any diagnostic application.

Towards this goal of nanoparticle assisted separations in gel, which can also be used for isolating the miRNA, mRNA, and ctDNA from a raw sample (Slouka et al., 2014), we report a proof-of-concept platform to detect and quantify short nucleic acids through induced nanoparticle aggregation and separation. Our technique relies on the ion-selective properties of ion-exchange membranes which are nanoporous and possess fixed positive or negative charges. The ion-selectivity of these membranes produces unique ion depletion and enrichment concentration polarization phenomena in their vicinity. Our group previously attached single-stranded DNA probes to anion-exchange membranes and demonstrated significant effects of hybridized targets on the concentration polarization phenomena to produce strong current-voltage signals (Slouka et al., 2013) leading to the detection of miRNA biomarkers for oral and pancreatic cancers (Senapati et al., 2014; Taller et al., 2015). Furthermore, the membrane's analyte enrichment capabilities improve the sensitivities and limits of detection in our microfluidic devices (Slouka et al., 2014). Other groups used the ion depletion front, with different ion conductivity across it, to isotachophoretically concentrate molecules in microfluidic channels (Quist et al., 2011, 2012) and paper media (Gong et al., 2015). Here, we integrate the analyte concentration and isotachophoretic depletion front generation with the molecular isolation and nanoparticle separation capabilities of the gel medium to perform selective field-induced aggregation of linked nanoparticles from a DNA sandwich assay.

Short nucleic acid targets are particular amenable to sandwich assays, wherein two different probe-functionalized gold nanoparticles link together through a common target to form

nanoparticle dimers, because long targets and probes tend to collapse and encapsulate the nanoparticles and suppress dimerization (Gagnon et al., 2008). Typical nanoparticle dimerization also suffers from diffusion limitations and hence requires long assay times for low analyte concentrations with a typical assay requiring overnight incubation for a target concentration of 20 nM (Elghanian et al., 1997). We use electrophoresis to pack the target and the particles against a cation-exchange membrane to both concentrate particles and achieve rapid target hybridization. After packing, we reverse the field, drive the nanoparticles in the opposite direction, and simultaneously form the depletion region. When the depletion front reaches the nanoparticles, it induces selective aggregation of the dimer particles while isotachophoretically driving the monomer particles down the channel. We then optically quantify the plasmon resonance band of the dimer particles to measure the DNA target concentration. Our technique quantifies the target within minutes and avoids the many arduous and hours-long steps involved in lab-based techniques such as Southern and Northern blotting. Additionally, the high electric fields formed by the depletion region create high shear forces to prevent nonspecific binding thus shortening the assay time. Here we demonstrate only single target detection but extension to multiple targets using nanoparticles with different plasmonic frequencies should be easily achievable.

## 2. Materials and methods

### 2.1. Materials

Fluorescein sodium salt was obtained from Fisher Scientific. Sodium chloride, sodium citrate, and chloroauric acid trihydrate were obtained from Sigma-Aldrich. Buffers were prepared by dilution from 10 X PBS (pH 7.4) and 50 X TAE (pH 8.4) obtained from Boston Bioproducts and 150 mM sodium phosphate buffer (pH 7.2) obtained from Teknova. Agarose gels were prepared at 1 wt% in 1 X TAE using agarose powder from Ominpur and stored as liquids inside an oven maintained at 65 °C. All agarose gels containing fluorescein were prepared in a like manner with the fluorescein concentration equal to 10 μM. QuikCast polyurethane casting resins (side A and side B) were obtained from TAP Plastics Inc. Acrifix 1R 0192 UV reactive cement was obtained from Evonik Industries while Loctite 3492 light cure adhesive was obtained from Loctite Corporation. Custom single stranded DNA probes and target sequences were used as received from Integrated DNA Technologies Inc. The two probe sequences were 5'/TGG TTC TCT CCG AAA TAG CTT TAG GG TA/3' for probe 1 and 5'/GAA GGG AAG AGG AAG AGG CAG GTG TCC TGT GGT AG/3' for probe 2. Probe 1 possessed a thiol modification at the 5' end while probe 2 possessed a thiol modification at the 3' end. The target sequence was 5'/CT ACC ACA GGA CAC CTG CCT CTT CCT CCC TTC AAAAA TA CCC CTA AAG CTA TTT CGG AGA GAA CCA/3' while the nontarget sequence was 5'/GCT GGC ACT CTA CAC TAG AAG GGA TAG ATA TGC CAA AAA AAC CAA ATT TCA GGC CCG GAA CTT TCT TGC/3'. The DNA probes and nontarget were dissolved in water to concentrations of 1 mM while the target DNA were dissolved in water to concentrations of 0.1 mM. All DNA samples were stored in a freezer at -4 °C until ready for use. Cation-exchange membranes whose fixed negative charge is supplied by organosulfonate groups were provided by Mega a.s (Czech Republic).

### 2.2. Synthesis and functionalization of Au nanoparticles

For detailed information on nanoparticle synthesis and probe functionalization, see Supporting Information Section 2.2. Gold nanoparticles were prepared by standard citrate reduction (Brown

et al., 2000). They were sized by a Malvern Nano-ZS Zetasizer and found to be approximately 20 – 30 nm in diameter. Their concentration was 2 nM as determined by UV-Vis spectroscopy (Haiss et al., 2007) using a Thermo Scientific NanoDrop 2000 spectrophotometer.

The particles were functionalized with DNA probes 1 and 2, in separate solutions, by gold-thiol bonding as described elsewhere (Demers et al., 2000). The final nanoparticle concentration was approximately 8 nM. DNA target solutions from 1  $\mu$ M down to 10 pM were prepared by mixing equal amounts of probe 1 and 2 nanoparticles followed by adding DNA targets. A nontarget solution was prepared in a like manner at 10  $\mu$ M. Heterogeneous mixtures were also prepared with concentrations of 1 nM target/10  $\mu$ M nontarget and 100 pM target/1  $\mu$ M nontarget. The solutions were mixed vigorously and incubated for at least twelve hours before use.

### 2.3. Chip fabrication

For detailed information regarding chip fabrication and design, see supporting information Section 2.3. Microfluidic chips were fabricated from 300  $\mu$ m polycarbonate sheets in a layer-by-layer fashion forming a single, straight channel with dimensions 2 mm width  $\times$  60 mm length  $\times$  500  $\mu$ m height. At either end of the channel were inlet/outlet holes for fluid and liquid gel. A 2 mm  $\times$  2 mm square hole for inserting the sample lay 10 mm from the inlet and between the inlet and the membrane. Another 6.9 mm diameter hole whose center was 10 mm away from the sample hole held the membrane cast. The cation-exchange membrane was sealed to the bottom of the cast and remained flush with the top of the microfluidic channel. The chip schematic is shown in Fig. 1c.

### 2.4. Separation and detection protocol

Chips were filled with agarose gel and used after the gel solidified. The gel occupying the sample reservoir was removed and filled with 2  $\mu$ L nanoparticle/DNA sample. The fluid reservoirs

were all filled with 1 X TAE buffer. Gel electrophoresis was conducted using a Keithley 2400A Sourcemeter with platinum electrodes as the voltage source. The protocol consisted of four steps: enrichment, depletion, expulsion, and repacking. 1) During enrichment, shown in Fig. 1a, the positive electrode was placed inside the membrane reservoir while ground was placed inside the inlet reservoir, and the sample was electrophoretically driven towards the membrane for five minutes by a 150 V potential. The particles required approximately one minute to reach the membrane at which point the sample reservoir was refilled with agarose gel. 2) During depletion, typically eight to nine minutes, the field was reversed by changing the electrode potential in the membrane reservoir to  $-150$  V. As shown in Fig. 1b, this generated a depletion front causing aggregation of one fraction of the nanoparticles while forcing away the remainder back towards the sample loading reservoir. 3) Expulsion was conducted by transferring the electrode in the membrane reservoir to the sample reservoir for one minute and forcing the particles therein into the region between the sample and inlet reservoirs. 4) In the repacking step, the field was reversed again with the positive electrode at 150 V in the membrane reservoir and the ground in the sample reservoir. The aggregated nanoparticles were concentrated and repacked against the membrane. From sample loading to target detection, the total time required was sixteen minutes.

The nanoparticles were imaged using a QImaging Retiga 2000R Fast 1394 camera and custom MATLAB programming. Images were recorded before the enrichment and depletion steps and after the repacking step. The particles near the membrane were quantified using the mean pixel intensity as measured by ImageJ. The fraction of aggregated particles was then calculated by taking the ratio of the intensity after repacking to the intensity after enrichment.

### 2.5. SEM analysis

In order to confirm the state of aggregation of the nanoparticles, SEM images of the two different bands were collected. To carry out the collection, a special chip was used where clear packaging tape replaced the bottom surface. After the depletion

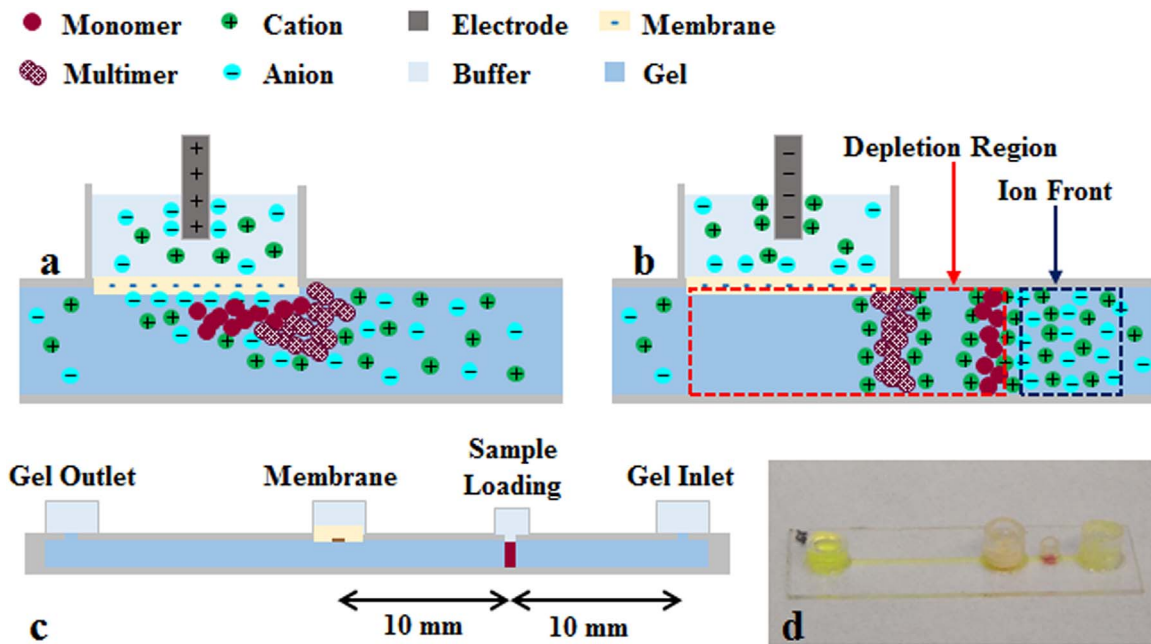


**Fig. 1.** Mechanism of nanoparticle separation. a) Enrichment: An electric field drives the particles towards the membrane and packs them at its surface. b) Depletion: The field is reversed, a depletion region forms, and the multimer particles aggregate while the monomer particles are driven away. c) Side view schematic of entire microfluidic chip. d) Chip filled with fluorescein-doped agarose gel and nanoparticles in the sample reservoir.

step separated the nanoparticles, the tape was peeled off, the two bands were cut from the gel, and then they were placed into separate containers in 20  $\mu\text{L}$  of water. The solutions were heated at 60 °C for twenty minutes to melt the gel. The solutions were then dispensed onto silicon substrates and evaporated. Following evaporation, the substrates were washed with water to remove any residual salt. The dried particles were imaged by a Carl Zeiss EVO-50 SEM. The subsequent images were analyzed in ImageJ using the “Analyze Particles” function to determine the area of the particles from which the diameter was then calculated.

### 3. Results and discussion

#### 3.1. Hybrid membrane-gel electrophoresis

Ion concentration polarization by the cation-exchange membrane is an essential feature of our new detection strategy. A positive potential applied above the membrane electrophoretically drives anions and negatively charged gold particles to accumulate at the surface because fixed negative charges prevent any negatively charged entity from passing through due to electrostatic repulsion. On the other hand, cations pass through freely leading to an enrichment effect beneath the membrane surface as in Fig. 1a. When the applied potential becomes negative, both cations and anions migrate away from the enriched region leaving behind a zone depleted of ions. Because the system must maintain electroneutrality, cations encounter the anions at the head of the depletion region and form the concentrated ion front illustrated in Fig. 1b. High voltages produce an extended space-charge region which forms a vortex instability that mixes the bulk electrolyte with the depletion zone and increases the current (Chang et al., 2012). In our system however, the gel suppresses vortex formation.

Hence, the depletion region migrates down the channel creating a sharp boundary between the depletion region and the ion front as shown by the fluorescein doped gel in supplementary information Fig. S-1. In the figure, the depletion is easily monitored by tracking the movement of the bright green fluorescein ions next to the dark, depleted region. As shown in the inset, the current falls dramatically due to lack of charge carriers in the depletion region. The drop in current places a high-field and a low-field region adjacent to each other and therefore facilitates an isotachophoretic separation front and avoids the tedious task of loading the channel with two different conductivity buffers. As we discuss later in more detail, this isotachophoretic front is responsible for the selective aggregation of DNA-linked nanoparticles.

For this proof-of-concept study, we used a combination of probe-functionalized gold nanoparticles, cation-exchange membranes, and gel electrophoresis to isolate and detect specific DNA sequences. An example separation of 100 nM target is illustrated in Fig. 2. In Fig. 2b, the nanoparticles pack at the membrane surface during enrichment. In Fig. 2c, the depletion causes the linked particles to aggregate whereas the uncaptured particles continue their migration back up the channel. As mentioned above, we also perform expulsion and repacking steps as in Fig. 2d which is necessary at low concentrations to enhance sensitivity and increase signal strength. Fig. 2 demonstrates a clear separation between targets and unlinked particles in less than 5 mm of channel length and less than seventeen minutes between sample loading and detection. We isolate the nanoparticle signal by image subtraction and set a threshold to avoid measurement noise. Our assay detects down to 10 pM which is approximately 10 million copies with our sample volume. Our result is comparable to previous isotachophoretic platforms with gel filters that report detection of 300 million copies of miRNA (Garcia-Schwarz and Santiago, 2012). Electrochemical methods such as differential pulse voltammetry

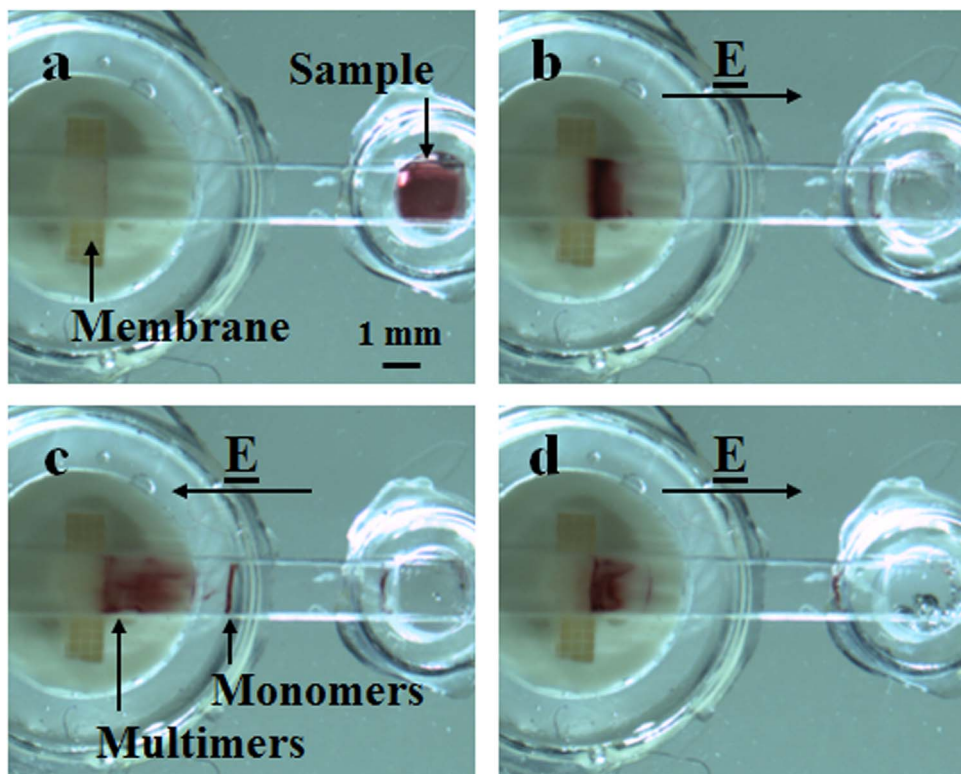


**Fig. 2.** Example separation of sample with 10 nM target. a) Nanoparticle/DNA mixture is inserted into sample inlet. b) Sample packs tightly against the membrane during the enrichment step. c) Five minutes into the depletion step, the uncaptured monomer particles separate from the now aggregated multimer particles linked by target molecules. The monomer particles continue to migrate up the channel as a thin line at the front of the depletion region. d) The aggregated particles are repacked against the membrane for detection.

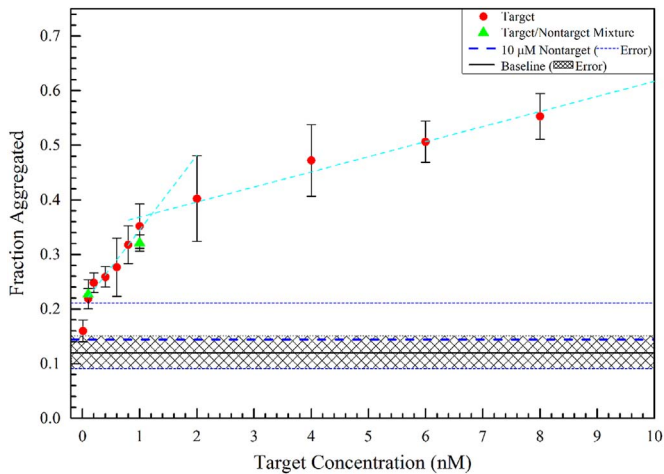


**Fig. 3.** Calibration curve showing the fraction of aggregation as a function of DNA concentration. The target/nontarget mixture points possess a nontarget-to-target ratio of 10,000:1. The baseline signal corresponds to the nanoparticle mixture without either target or nontarget. Linear fits are shown from 100 pM to 1 nM and 1 nM to 8 nM with correlation coefficients of 0.96 and 0.98, respectively. Error bars represent uncertainties within a 95% confidence interval and  $n=4$ .

report detection limits that vary from 800 pM (Luo et al., 2013) to 2 pM (Li et al., 2015) down to 0.4 fM (Jia et al., 2016) and 0.2 fM (Pan et al., 2015). Although these biosensors report lower limits of detection, they typically rely on diffusion-based hybridization. Hence, they report assay times from one hour up to five hours, particularly at low concentrations. In contrast, our assay requires less than twenty minutes from sample loading to detection. In addition, electrochemical sensors employ expensive fabrication methods and tedious preparation of electrodes making them unsuitable for point-of-care applications.

Following this procedure, we established the calibration curve in Fig. 3 for the 10 pM to 10 nM range. First, Fig. 3 shows our system is highly selective between targets and nontargets. It should be noted that there is a small amount of aggregation despite the absence of any DNA targets or nontargets, and this is the baseline signal of our platform, yet we detect down to 10 pM target above the baseline. On the other hand, even at 10  $\mu$ M, the signal from the nontarget is, within error, equivalent to the baseline. Furthermore, we maintain the signal intensity in heterogeneous mixtures where the nontargets outnumber the targets by a factor of 10,000 to 1. At 1 nM and 100 pM, the mixture's signal is identical to the signal from pure target thereby demonstrating the selective nature of our assay and its potential use for complex media. Second, the graph reveals two linear regimes: one from 100 pM to 1 nM and one from 1 nM to 8 nM with correlation coefficients of 0.96 and 0.98, respectively, for the lines of best fit. The ratio of nanoparticles to target molecules explains the presence of these two regimes and the decrease in sensitivity between 1 and 8 nM. In an ideal scenario, each target links a nanoparticle to only one other nanoparticle and forms them into dimers. However, in practice, targets link nanoparticles into trimmers, tetramers, and higher multimers. At low target concentrations, when the ratio of nanoparticles to targets is large, the probability to form dimers is much higher. At a concentration of 8 nM gold nanoparticles, the nanoparticle to target ratio goes from 800:1 to 8:1 in the 100 pM to 1 nM range, respectively, and is significant enough to form mainly dimers. Above 1 nM, the ratio approaches and then falls below 1:1 so that multimer formation becomes more probable. The concentration range where dimers form is more sensitive because each additional target corresponds to an additional two nanoparticles. In contrast, in the multimer regime there is a greater probability that targets will hybridize to particles already

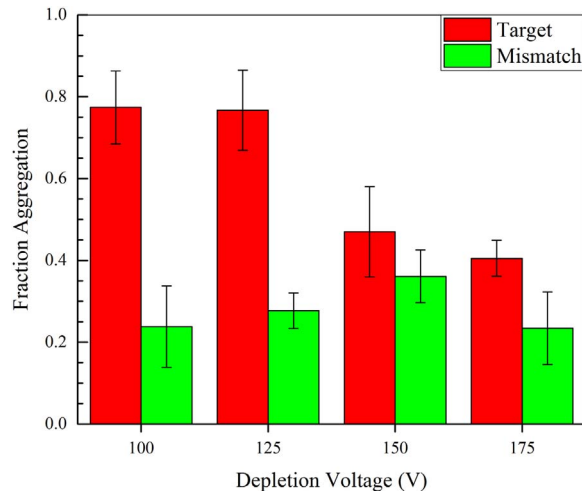


**Fig. 4.** Selectivity of the sensor for fully complementary target versus two-base pair mismatch target. The depletion voltage was initially applied at  $-200$  V potential for one minute followed by a step to change to different lower voltages. Error bars represent uncertainties within a 95% confidence interval and  $n=4$ .

linked as dimers. Therefore, there is a smaller increase in the signal and consequently lower sensitivity. The changing sensitivity with the nanoparticle to target ratio demonstrates the scalability of our platform. That is, we can potentially lower the limit of detection by decreasing the concentration of the nanoparticles at low target concentrations to obtain higher order multimers and hence more severe aggregation. It follows that we may also increase the dynamic range by careful adjustment of the nanoparticle concentration depending on the amount of target present in the sample. This could be achieved by testing multiple channels with different nanoparticle concentrations simultaneously and then running subsequent measurements at only one concentration for greater precision. A future publication will more completely study the effects and performance of changing the nanoparticle to target ratio.

In Fig. 4, we provide preliminary results examining the selectivity of the sensor using targets with two base mismatches on each probe, so the target sequence becomes 5'/CTACCGT...GCAACCA/3'. The experiments were carried out using slightly altered conditions where the distance between the channel inlet and membrane reservoirs reduced to 15 mm, the enrichment time increased to six minutes, and the applied potential during depletion underwent a step change. We applied the maximum output of the sourcemeter,  $-200$  V, for one minute, and then we lowered the potential for the remainder of the depletion step (i.e. until the monomer reached the sample reservoir). In Fig. 4, we see the greatest selectivity when the potential is lowered to 100 V and obtain target to mismatch signal ratio greater than 3. Our results are comparable to other assays such as the NanoBioArray chip of Sedighi et al. (2014) based on hybridization of target-conjugated nanoparticles to surface-immobilized probes and the molecular beacon/Ag nanocluster technique of Cao et al. (2015) who report selectivity values of approximately 3 to 6 and 2-3, respectively. It is important to realize the mismatches occur in the middle of the probes rather than at the ends. Mismatches positioned in the middle may significantly reduce the selectivity (Cheng et al., 2010), yet we are still able to discriminate between them and the completely matched target. Although we do not offer a detailed explanation here, we also note the importance of changing the electric field strength on improving the selectivity. We intend to offer a more detailed and exhaustive study concerning the selectivity and the effects of numbers of mismatches as well as mismatch location in a future publication.

Our SEM analysis confirms the presence of monomers and multimers in the separated bands. In Fig. 4a, the SEM image of the monomer band demonstrates the dominant presence of monomer particles over dimers and higher multimers. The inset of Fig. 4a shows a histogram analysis of the diameters of over 1000 particles. The average particle diameter is 17 nm which corresponds well with the known diameters from dynamic light scattering. Very few particles possess diameters above 30 nm which would be indicative of the formation of dimers. In Fig. 4b though, large aggregates dominate over the presence of monomers. Although the histogram in the inset still shows some monomer particles, the distributions shifts significantly to higher diameters compared to the inset in Fig. 4a. The diameters of the aggregates may also be underestimated due to the decreasing circularity of the large aggregates. Moreover, during sample preparation, the heating stage which melts the gel may have denatured some of the hybridized pairs causing particle dissociation and thus resulting in more monomers. However, Fig. 4 clearly proves the depletion front aggregates linked particles but removes monomer particles.

### 3.2. Reducing hybridization time

We performed further experiments to examine the role enrichment plays in our assay by investigating how the enrichment time affects aggregation. For an 8 nM target sample, we carried out the enrichment step for various times beginning at one minute and increasing the time in one minute intervals up to twelve minutes. The subsequent depletion, expulsion, and repacking steps we performed as usual although the time required for the depletion step increased as the enrichment time increased. We show the results in Fig. S-2 in the supporting information. Overall, the fraction of aggregated particles increases linearly with the enrichment time although the data at one and two minutes fall below the baseline signal. Longer than six minutes, the slope decreases and finally begins to saturate at twelve minutes.

Other than reducing the diffusion time for nanoparticle linkages by concentrating the nanoparticles, the enrichment step also favorably affects the hybridization thermodynamics. The increasing aggregation shown in Fig. S-2 indicates increasing numbers of targets hybridize to the nanoparticles while packing near the membrane surface. This effect can be explained by examining the thermodynamic equilibrium surrounding the hybridization reaction. From Gong and Levicky (2008), the hybridization of a DNA target to a surface-bound probe can be written as  $T+P+JC \rightarrow D$  where  $T$  is the target,  $P$  is the probe, and  $D$  is the hybridized duplex. The  $J$  term accounts for a number  $J$  of cations,  $C$ , which are initially free in solution but associate to the duplex to screen the increased charge density on the DNA duplex. The equilibrium expression is then

$$\frac{[D]}{[T][P][C]^J} = \frac{1}{K_D}$$

where  $K_D$  is the dissociation constant. Because target molecules and cations are small compared to the size of the nanoparticles, we expect them to concentrate more than the nanoparticles which, by the surface bound nature of the probes, effectively control the probe and duplex concentrations. Therefore, the concentrations of targets and cations increase relative to the concentration of the duplexes and push equilibrium to favor hybridization. When we reverse the field and form the depletion, we expect the reverse reaction rate to increase. That is, we should see the dissociation of duplexes as targets and cations migrate away from the membrane. However, the depletion induces aggregation of the nanoparticles before significant dissociation ensues. So, although dehybridization is thermodynamically more favorable

during depletion, it is kinetically limited because of the aggregation. We effectively lower the dissociation constant by the combined effects of enrichment and depletion. This result is particularly encouraging since target hybridization to surface-based probes tends to be less favorable than solution-based probes (Levicky and Horgan, 2005; Ravan et al., 2014).

We see further proof that hybridization takes place during the enrichment step by comparing the aggregation between targets hybridized on-chip and targets hybridized off-chip. For on-chip hybridization, we prepared 100 nM target samples, vortexed them briefly, and then immediately analyzed them using our protocol. For off-chip hybridization, we simply used our normal samples with twelve hour hybridization. We also compared the aggregation to a 10  $\mu$ M nontarget sample hybridized on-chip and samples with no target. The fractional aggregation for on-chip hybridization is identical to that for off-chip hybridization disposing of the need for the hours-long incubation step. Additionally, there is no significant aggregation from the nontarget DNA sample, so no selectivity is lost. Therefore, we can achieve rapid, selective hybridization on-chip and significantly reduce the total analysis time to less than twenty minutes. The enrichment concentrates the target which increases the reaction rate and thereby overcomes the kinetic limitations and the transport-limited hybridization reaction in the bulk.

### 3.3. Mechanism for selective field-induced nanoparticle aggregation by the depletion front

It is quite apparent from Figs. 3 and 5 that the depletion front induces nanoparticle aggregation only for linked nanoparticles. Field induced nanoparticle dipoles are known to induce aggregation (Hermanson, 2001; Klopper et al., 2004), but it is unclear why only linked particles aggregate in our platform. To elucidate the mechanism behind this curious selective aggregation, we conducted another experiment wherein we used fluorescein doped gel to track the movement of the depletion region and simultaneously monitor the aggregation and separation of the nanoparticles. As we expect, the separation does not take place until the depletion region reaches the nanoparticles; after the separation, the monomers remain isotachophoretically packed against the depletion front and carried by the front downstream. This experiment is repeated with a series of pauses during the depletion step. Images simultaneously displaying the fluorescence-tracked depletion and the nanoparticles are shown in Fig. 6 while the nanoparticles' position is confirmed by bright field images (not shown). Fig. 6a shows the nanoparticles' initial position at the beginning of the depletion step while Fig. 6b shows them three minutes later just as the depletion front begins to form. Here, we introduce the first pause before any separation. Each pause lasts fifteen minutes, and during this time, the fluorescein diffuses into the depletion region as in Fig. 6c. We reapply the voltage for one minute and then allow another fifteen minute pause. When we reapply the voltage, the depletion region quickly reforms, and overtakes the nanoparticles in Fig. 6d. The fluorescein again diffuses into the depletion region in Fig. 6e until we apply the voltage for another minute to yield the final image, Fig. 6f, where the gap between the nanoparticles and the depletion front becomes very obvious. We note first that the nanoparticles no longer migrate under the applied field indicating aggregation. Second, no separation exists between hybridized and unhybridized nanoparticles, indicating the aggregation of both monomer (unhybridized) and multimer (hybridized) particles.

Results obtained from Fig. 6 reveal the crucial role of depletion ramping in inducing selective aggregation, and we explain them through depletion induced isotachophoretic separation. Separation by depletion isotachophoresis was actually first reported only

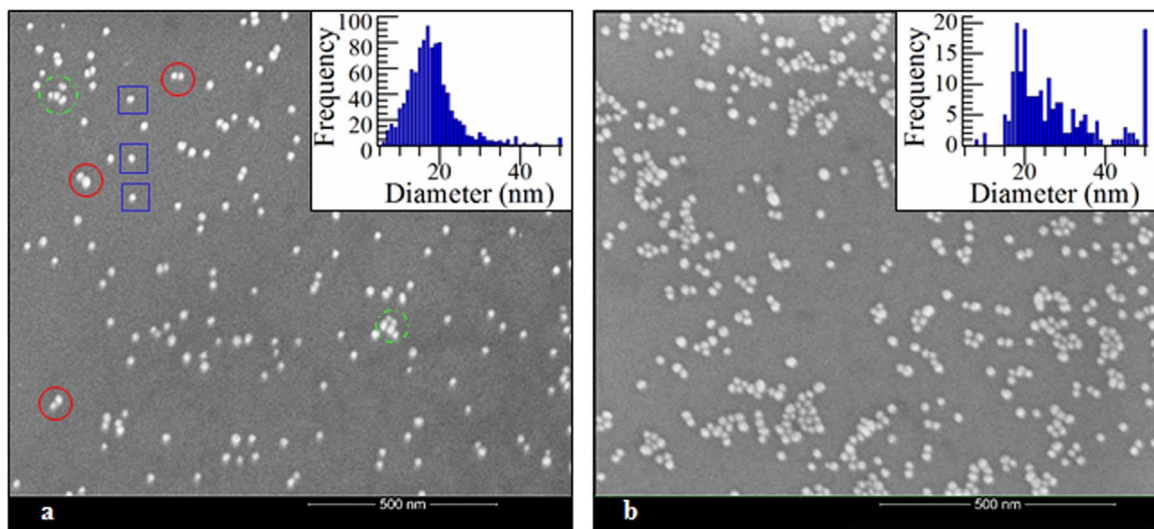


**Fig. 5.** SEM images of nanoparticles from the a) monomer band and b) aggregated band. Examples of different types of particles in part a are monomers shown by blue squares, dimers by red circles, and larger aggregates by broken green circles. The insets are representative histograms of particle diameters from each respective band. (For interpretation of the references to color in this figure legend, the reader is referred to the web version of this article.)

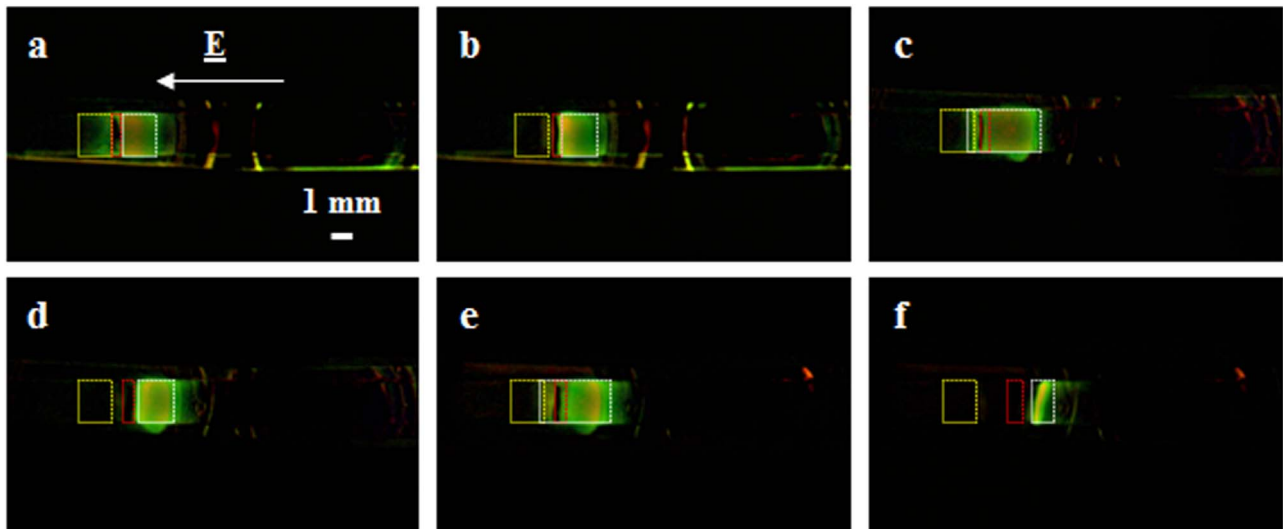


**Fig. 6.** Depletion step in fluorescein doped gel. Positions of the membrane, nanoparticles, and ion front are indicated by the yellow, red, and white boxes, respectively. The depletion front, indicated by the concentrated fluorescein band, was isolated by image subtraction. Images were taken after a) 0 min, b) 3 min applied voltage, c) 15 min no voltage, d) 1 min applied voltage, e) 15 min no voltage, and f) 1 min applied voltage. (For interpretation of the references to color in this figure legend, the reader is referred to the web version of this article.)

recently by Quist et al. (2011, 2012) for fluorescent analytes. As explained in Fig. S-1, the formation of the depletion region leads to a rapid drop in current which in turn creates a high electric field. At the same time, ions accumulate just ahead of the depletion front. A very sharp electric field gradient develops between the high electric mobility environment in the depletion region and the low electric mobility environment in the concentrated ion front. The adjacent high and low electric mobility environments facilitate the proper conditions for an isotachophoretic separation without using immiscible solvents with different ionic strengths. The linked and unlinked nanoparticles possess enough of a mobility difference to separate within the isotachophoretic region. However, such a separation is feasible only with a continuous depletion front with all the nanoparticles initially packed at the membrane. We determine this from the stop/start experiment illustrated in Fig. 6. The fluorescein ions quite obviously diffuse into the depletion region. Although it is not readily apparent, we can assume the monomer and dimer particles also diffuse and mix

with each other. Once we reapply the voltage, however, the particles do not have enough time to separate before the depletion overtakes them. Therefore, when the dimer particles aggregate, the monomer particles become trapped within the aggregated complex as well. When we let the depletion run continuously instead, we see aggregation of only the linked particles. With a continuous depletion front, the band of separated, linked dimers are in the high field region at the isotachophoretic front and the band of unlinked nanoparticles are in the high ionic strength, low field region just ahead. The large field gradient within the isotachophoretic front hence induces selective aggregation of the linked nanoparticles in the back of the front and not the unlinked nanoparticles at the front only if the two sets of particles are separated at the isotachophoretic front with continuous depletion.

We have shown that the dimerization of the particles in the advancing depletion front occurs only if the particles are linked by a single target molecule. We believe this is due to a selective and irreversible aggregation kinetic mechanism in the presence of a

decaying electric field. Wijenayaka et al. (2015) recently performed extensive characterization of the interparticle interactions between Au nanoparticles functionalized with negatively charged ligands using an extended DLVO theory. The dominant interactions between the particles are the repulsive electrostatic forces and the attractive van der Waals (vdW) forces. Wijenayaka et al. showed that our smaller particles ( $< 50$  nm) have higher Hamaker constants. The result is that for conditions where spontaneous aggregation does not occur, a potential barrier more than  $10 k_B T$  exists at roughly a few nanometers of particle separation due to a balance between these two opposing interactions but both interactions will vanish more than 10 nm away (Wijenayaka et al., 2015). The linking target molecule can reduce this barrier because of the preferred association of free polyvalent cations around the duplex (Gong and Levicky, 2008) that screen the electrostatic repulsion between the negatively charged particles. This aggregation barrier can be lowered significantly or even eliminated entirely by imposing a sufficiently high electric field (Liu et al., 2013) due to an attractive interaction between the two induced nanoparticle dipoles. How much the barrier is lowered by the electric field can be estimated by the voltage drop across the separation where the barrier lies (a few nanometers). Most of the 150 V voltage drop is in the depleted region and hence when the depletion front has only advanced a few millimeters, the voltage drop across the barrier separation of a few nanometers can be as large as  $10 k_B T$  but it decays to below  $1 k_B T$  when the front has advanced more than 1 cm. The barrier for linked particles hence disappears and appears in less than one minute between the time the depletion region hits the particles and the time it passes them. The particles would aggregate spontaneously without the barrier because the linker particles keep them within 10 nm of each other to allow rapid attractive interaction. The unlinked particles either still have a significant barrier during this interval or are too far apart to aggregate within the interval. This is then the role of the linking target molecules—their cations lower the barrier, so it can be removed by the electric field for an interval in time, and they tether the two linked nanoparticles so they are driven irreversibly by the attractive vdW force in that interval.

#### 4. Conclusion

We developed a new detection and quantification protocol for short single-stranded nucleic acids which uses the enrichment and depletion features of a cation-exchange membrane to isolate gold nanoparticle reporters with captured DNA targets during depletion-generated gel isotachophoresis. Our microfluidic chip detects single-stranded DNA targets down to 10 pM within a 2  $\mu$ L sample volume. One key component, the enrichment, helps achieve rapid hybridization while also effectively lowering the dissociation constant to increase the number of hybridized targets. The crucial features of the other key component, the depletion, are creating a sharp electric field gradient to isotachophoretically separate the linked and unlinked particles and then selectively aggregating the linked particles. The assay is highly selective against nontargets even when such nontargets significantly outnumber targets in heterogeneous mixtures. Unlike lateral flow assays, we retain a method to remove nontarget molecules and increase specificity; that is, the depletion region creates a high electric field which removes nonspecific binding. Our gel platform can also be readily integrated with other gel systems such as those which purify nucleic acids from proteins and large cell debris from lysate. Our group previously developed a gel-based filter which selectively passed short nucleic acids while blocking the passage of proteins and cell debris (Slouka et al., 2013, 2014; Egatz-Gomez et al., 2016). Therefore, nucleic acids purified from blood or serum will not

suffer from fouling of nonspecific interactions caused by undesirable components.

As a proof-of-concept study, the microfluidic chip we presented here is largely unoptimized. We expect to improve sensitivity and attain lower limits of detection as well as increase the dynamic range by decreasing the microchannel's dimensions, employing better optical detectors, and scaling the nanoparticle concentration with the target concentration. In addition, there are many variables, such as the buffer concentration, the electric field strength, the nanoparticles' size and concentration, target length, etc, which affect how much aggregation takes place as well as when and where it occurs, so they must be studied systematically to determine the optimal parameters for maximum aggregation. We can also transition to multitarget sensing by incorporating different types of nanoparticles into the assay. These could be other plasmonic nanoparticles such as silver and nickel, or they could be fluorescently doped silica particles. Differences in electrophoretic mobility could result in DNA barcodes, but even mixed aggregation where the particles overlap is still useful with a simple spectrometer. We can hence, in principle, identify and quantify multiple short nucleic acids without the tedious and time-consuming steps of blotting, pretreatment for PCR, or long microarray assay time for genomic liquid biopsies.

#### Acknowledgments

Thanks are due to Ceming Wang for obtaining SEM images of the nanoparticles. We also express our gratitude for funding to the Naughton Foundation and to NSF-CBET1065652.

#### Appendix A. Supporting information

Supplementary data associated with this article can be found in the online version at <http://dx.doi.org/10.1016/j.bios.2016.07.093>.

#### References

- de Avila, B.E.F., Watkins, H.M., Pingarron, J.M., Plaxco, K.W., Palleschi, G., Ricci, F., 2013. *Anal. Chem.* 85 (14), 6593–6597.
- Brown, K.R., Walter, D.G., Natan, M.J., 2000. *J. Chem. Mater.* 12, 306–313.
- Calin, G.A., Croce, C.M., 2006. *Nat. Rev. Genet.* 6, 857–866.
- Cao, Q., Teng, Y., Yang, X., Wang, J., Wang, E., 2015. *Biosens. Bioelectron.* 74, 318–321.
- Chang, H.-C., Yossifon, Y., Demekhin, E.A., 2012. *Annu. Rev. Fluid Mech.* 44, 401–426.
- Cheng, I.F., Senapati, S., Cheng, X., Basuray, S., Chang, H.C., Chang, H.C., 2010. *Lab Chip* 10, 828–831.
- Chua, A., Yean, C.Y., Ravichandran, M., Lim, B., Lalitha, P., 2011. *Biosens. Bioelectron.* 26, 3825–3831.
- Corstjens, P.L.A.M., Zuiderveld, M., Nilsson, M., Feindt, H., Niedbala, R.S., Tanke, H.J., 2003. *Anal. Biochem.* 312, 191–200.
- Demers, L.M., Mirkin, C.A., Mucic, R.C., Reynolds, R.A., Letsinger, R.L., Elghanian, R., Viswanadham, G., 2000. *Anal. Chem.* 72, 5535–5541.
- Egatz-Gomez, A., Wang, C., Klacsmann, F., Pan, Z., Marczak, S., Wang, Y., Sun, G., Senapati, S., Chang, H.C., 2016. *Biomicrofluidics* 10, 032902.
- Elghanian, R., Storhoff, J.T., Mucic, R.C., Letsinger, R.L., Mirkin, C.A., 1997. *Science* 277 (5329), 1078–1081.
- Fang, Z., Ge, C., Zhang, W., Lie, P., Zeng, L., 2011. *Biosens. Bioelectron.* 27, 192–196.
- Gagnon, Z., Senapati, S., Gordon, J., Chang, H.C., 2008. *Electrophoresis* 29, 4808–4812.
- Gao, X., Xu, H., Baloda, M., Gurung, A.S., Xu, L., Wang, T., Zhang, X., Liu, G., 2014. *Biosens. Bioelectron.* 54, 578–584.
- Garcia-Schwarz, G., Santiago, J.G., 2012. *Anal. Chem.* 84, 6366–6369.
- Gong, P., Levicky, R., 2008. *PNAS USA* 105 (14), 5301–5306.
- Gong, M.M., Nosrati, R., San Gabriel, M.C., Zini, A., Sinton, D., 2015. *J. Am. Chem. Soc.* 137, 13913–13919.
- Haiss, W., Thanh, N.T.K., Aveyard, J., Fernig, D.G., 2007. *Anal. Chem.* 79, 4215–4221.
- Hampl, J., Hall, M., Mufiti, N.A., Yao, Y.M., MacQueen, D.B., Wright, W.H., Cooper, D.E., 2001. *Anal. Biochem.* 288, 176–187.
- Hanauer, M., Pierrat, S., Zins, I., Lotz, A., Sonnichsen, C., 2007. *Nano Lett.* 7 (9), 2881–2885.
- He, Y., Zhang, S., Zhang, X., Baloda, M., Gurung, A.S., Xu, H., Zhang, X., Liu, G., 2011.

- Biosens. Bioelectron. 26, 2018–2024.
- Hermanson, K.D., Lumsdon, S.O., Williams, J.P., Kaler, E.W., Velev, O.D., 2001. Science 294 (5544), 1082–1086.
- Hlavacek, A., Skladal, P., 2012. Electrophoresis 33, 1427–1430.
- Hlavacek, A., Sedlmeier, A., Skladal, P., Gorris, H.H., 2014. Appl. Mater. Interfaces 6, 6930–6935.
- Hou, S.Y., Hsiao, Y.L., Lin, M.S., Yen, C.C., Chang, C.S., 2012. Talanta 99, 375–379.
- Hu, J., Wang, L., Li, F., Han, Y.L., Lin, M., Lu, T.J., Xu, F., 2013. Lab Chip 13, 4352–4357.
- Jia, L., Shi, S., Ma, R., Jia, W., Wang, H., 2016. Biosens. Bioelectron. 80 (392–297).
- Kim, J.Y., Kim, H.B., Jang, D.J., 2013. Electrophoresis 34, 911–916.
- Kloepfer, K.D., Onuta, T.D., Amarie, D., Dragnea, B., 2004. J. Phys. Chem. B 108, 2547–2553.
- Li, Z., Miao, X., Xing, K., Zhu, A., Ling, L., 2015. Biosens. Bioelectron. 74, 687–690.
- Liu, F.K., Wei, G.T., 2004. Anal. Chim. Acta 510, 77–83.
- Liu, F.K., Ko, F.H., Huang, P.W., Wu, C.H., Chu, T.C., 2005. J. Chromatogr. A 1062, 139–145.
- Liu, F.K., 2009. J. Chromatogr. A 1216, 9034–9047.
- Liu, S., Yan, Y., Wang, Y., Senapati, S., Chang, H.C., 2013. Biomicrofluidics 7, 061102.
- Levicky, R., Horgan, A., 2005. TRENDS Biotechnol. 23 (3), 143–149.
- Lujambio, A., Lowe, S.W., 2012. Nature 482, 347–355.
- Luo, X.W., Du, F.J., Wu, Y., Gao, L.J., Li, X.X., 2013. Chin. J. Anal. Chem. 41 (11), 1664–1668.
- Mao, X., Ma, Y., Zhang, A., Zhang, L., Zeng, L., Liu, G., 2009. Anal. Chem. 81, 1660–1668.
- Moghadam, B.Y., Connelly, K.T., Posner, J.D., 2015. Anal. Chem. 87, 1009–1017.
- Pan, H., Yu, H., Wang, N., Zhang, Z., Wan, G., Liu, H., Guan, X., Chang, D., 2015. J. Biotechnol. 214, 133–138.
- Parolo, C., Escosura-Muniz, A., Merkoci, A., 2013. Biosens. Bioelectron. 40, 412–416.
- Praus, P., Turicova, M., Suchomel, P., Kvitek, L., 2015. RSC Adv. 5, 59131–59136.
- Pyell, U., Bucking, W., Huhn, C., Herrmann, B., Merkulov, A., Mannhardt, J., Jungclas, H., Nann, T., 2009. Anal. Bioanal. Chem. 395, 1681–1691.
- Quist, J., Janssen, K.G.H., Vulto, P., Hankemeier, T., van der Linden, H., J., 2011. Anal. Chem. 83, 7910–7915.
- Quist, J., Vulto, P., van der Linden, H., Hankemeier, T., 2012. Anal. Chem. 84, 9065–9071.
- Ravan, H., Kashanian, S., Sanadgol, N., Badoei-Dalfard, A., Karami, Z., 2014. Anal. Biochem. 444, 41–46.
- Rohrman, B.A., Leautaud, V., Molyneux, E., Richards-Kortum, R.R., 2012. PLoS One 7 (9), e45611–e45618.
- Sedighi, A., Li, P.C.H., Pekcevik, I.C., Gates, B.D., 2014. ACS Nano 8 (7), 6765–6777.
- Senapati, S., Slouka, Z., Shah, S.S., Behura, S.K., Shi, Z., Stack, M.S., Severson, D.W., Chang, H.C., 2014. Biosens. Bioelectron. 60, 92–100.
- Slouka, Z., Senapati, S., Yan, Y., Chang, H.C., 2013. Langmuir 29, 8275–8283.
- Slouka, Z., Senapati, S., Chang, H.C., 2014. Annu. Rev. Anal. Chem. 7, 317–335.
- Taller, D., Richards, K., Slouka, Z., Senapati, S., Hill, R., Go, D.B., Chang, H.C., 2015. Lab. Chip, 1656–1666.
- Traver, S., Assou, S., Scalici, E., Haouzi, D., Al-Edani, T., Belloc, S., Hamamah, S., 2014. Hum. Reprod. Update 20 (6), 905–923.
- Vogelstein, B., Papadopoulos, N., Velculescu, V.E., Zhou, S., Diaz Jr., L.A., Kinzler, K. W., 2013. Science 339, 1546–1558.
- Wijenayaka, L.A., Ivanov, M.R., Cheatum, C.M., Haes, A.J., 2015. J. Phys. Chem. C 119, 10064–10075.
- Wu, W., Huang, J., Wu, L., Sun, D., Lin, L., Zhou, Y., Wang, H., Li, Q., 2013. Sep. Purif. Technol. 106, 117–122.
- Xu, X., Caswell, K.K., Tucker, E., Kabisatpathy, S., Brodhacker, K.L., Scrivens, W.A., 2007. J. Chromatogr. A 1167, 35–41.